Silicon Photonic Mach–Zehnder Modulator Architectures for on Chip PAM-4 Signal Generation

Alireza Samani [ID], Eslam El-Fiky [ID], Mohamed Morsy-Osman [ID], Rui Li [ID], David Patel, Thang Hoang [ID], Maxime Jacques [ID], Mathieu Chagnon [ID], Nicolás Abadía, and David V. Plant, *Fellow, IEEE, Fellow, OSA*

Abstract—Four level pulse amplitude modulation (PAM-4) has become the modulation format of choice to replace ON–OFF keying (OOK) for the 400 Gb/s short reach optical communications systems. In this paper, we investigate the possible modifications to conventional Mach–Zehnder modulator structures to improve the system performance. We present three different silicon photonic Mach–Zehnder modulator architectures for generating PAM-4 in the optical domain using OOK electrical driving signals. We investigate the transfer function and linearity of each modulator and experimentally compare their PAM-4 generation and transmission performance with and without use of digital signal processing (DSP). We achieve the highest reported PAM-4 generation and transmission without the use of DSP. The power consumption of each modulator is presented, and we experimentally show that multielectrode Mach–Zehnder modulators provide a clear advantage at higher symbol rates compared to conventional Mach–Zehnder modulators.

Index Terms—Amplitude modulation, electrooptic modulators, optical interferometry, photonic integrated circuits, silicon photonics.

I. INTRODUCTION

SINCE the inception of the fiber optics communication, On-Off keying (OOK) has been the main modulation format employed in short reach optical interconnects. The simplicity of the transmitter and receiver architectures have been an important factor in the success of OOK for short reach optical links. Recently deployed 100 Gb/s systems utilize OOK modulation in 4×25 Gb/s configuration [1]. However, as we move towards

200 Gb/s and 400 Gb/s systems, OOK requires a proportional increase in the bandwidth, and hence a more efficient modulation format is required to avoid such complexity. This has created new challenges in developing power efficient, low cost transmitter optical sub-assemblies (TOSAs), and receiver optical sub-assemblies (ROSAs) for data centers which would fit into a compact quad small form-factor pluggable (QSFP), since any change in modulation format usually creates further complexities in developing the TOSA and ROSA. Consequently, various modulation formats with higher spectral efficiency such as discrete multi-tone (DMT) [2], 4-level pulse amplitude modulation (PAM-4) [2] and quadrature phase shift keying (QPSK) [3]–[5] have been studied to replace OOK. Recently, the 200 Gb/s and 400 Gb/s IEEE Ethernet standard has been released, and the PAM-4 modulation format has been selected for 400 Gb/s systems using 4 lanes of 100 Gb/s configuration or 8 lanes of 53.125 Gb/s for various target reaches [6]. Unlike QPSK, PAM-4 is a direct detect format and as such requires minimal change to the ROSA compared to OOK, however on the TOSA, a more significant update is required to generate the PAM-4 signal. In this manuscript we focus on different silicon photonic (SiP) travelling wave Mach Zehnder modulator (TWMZM) architectures which enable PAM-4 signal generation in the optical domain versus generating the PAM-4 signal in electrical domain.

Over the past few years, there has been significant work on PAM-4 generation using vertical-cavity surface-emitting lasers (VCSEL)s [7], [8], silicon photonic ring modulators [9]–[13], silicon-germanium electrooptic modulators [14], [15], III–V-on-silicon modulators [16] silicon hybrid modulators [17], TWMZMs [18]–[24], electro-optic polymer modulators [25] and LiNbO3 modulators [26]. In the majority of the presented works, PAM-4 is generated in the electrical domain either by passive power combination of two OOK signals or using digital to analog convertors (DACs) and digital signal processing (DSP). Additionally, most of the work have been done in the C-band while short reach transmission systems typically operate in the O-band.

In this paper, we present four O-band Silicon photonic (SiP) modulators based on 3 different Mach-Zehnder interferometer structures to generate multi-amplitude modulation formats. Each candidate is capable of 112 Gb/s PAM-4 transmission below the hard decision forward error correction (HD-FEC) threshold

of 3.8×10^{-3}. We investigate and compare the performance advantages of generating PAM-4 using various structures of MZM optically as opposed to generating PAM-4 in the electrical domain using conventional DACs and MZMs. The two variants of optical DACs are a dual parallel Mach-Zehnder modulator (DP-MZM) with one series push pull TWMZM on each arm, and a single MZM having two electrodes in series that we name multi-electrode MZM (ME-MZM). First, we present the optical design of the modulators and investigate the effects of non-linearities of the MZM transfer function and PN junction phase-shifters on performance of the PAM-4 generation. Next, we examine the effects of microwave loss and 3-dB bandwidth (BW) on the overall performance of the modulators. We use the simple figure of merit BW/V_π, to compare the performance of the modulators for specific baudrates and drive-voltages, where V_π is the voltage applied to the modulator to achieve π phase shift. Finally, we parametrically examine the transmission performance of each modulator and present an optimized modulator design for DAC -less and DSP less 112 Gb/s PAM-4 transmission. Furthermore, we present the highest transmitted symbol rate using an O-band SiP modulator reported to date.

II. DEVICE DESIGN, FABRICATION AND CHARACTERIZATION

We investigate the PAM-4 performance of three different types of Mach-Zehdner modulator structures namely the TWMZM, DP-MZM and ME-MZM. All modulators are designed and driven in series-push pull (SPP) scheme as detailed in [27], where a positive phase shift in one arm is accompanied by a negative phase shift of equal strength in the other arm. One advantage of the SPP MZM is that it requires one RF signal to drive the modulator. This noticeably lowers the system complexity, when operating the DP-MZM and the ME-MZM for PAM-4 modulations, since addition of any RF signal requires further microwave analysis and can trigger unwanted cross talk between channels. All presented modulators are designed for the transmission of 112 Gb/s PAM-4 on a single carrier. Consequently, the main target specification for our designs is to have EO bandwidth for each modulator $\geq$ 35 GHz. This benchmark bandwidth value is chosen based on the target baudrate, PAM-4 spectral efficiency and considering our transmission system components, such as RF amplifiers and photodetectors. It should be mentioned that, this bandwidth can be further optimized for specific symbol rate, and driver circuitry. To unbiasedly evaluate the performance of different modulator structures we use the same phase shifter and electrode design for all three types of modulators. As a result, we present four modulators as follows: a) TWMZM with 3 mm long phase shifter, b) a DP-MZM with 3 mm long inner TWMZMs, c) a ME-MZM with two, 1.5 mm long phase shifters and finally d) ME-MZM with two 3 mm long phase shifters. We present two ME-MZM variations to be able to unbiasedly compare the performance of the three types of modulators. The shorter ME-MZM has the same phase shifter length and hence the same $V\pi$ as the TWMZM and DP-MZM, while the longer ME-MZM has the same electrode length and hence similar bandwidth as the presented TWMZM and DP-MZM. The schematic of the modulators is shown in Fig. 1. Two
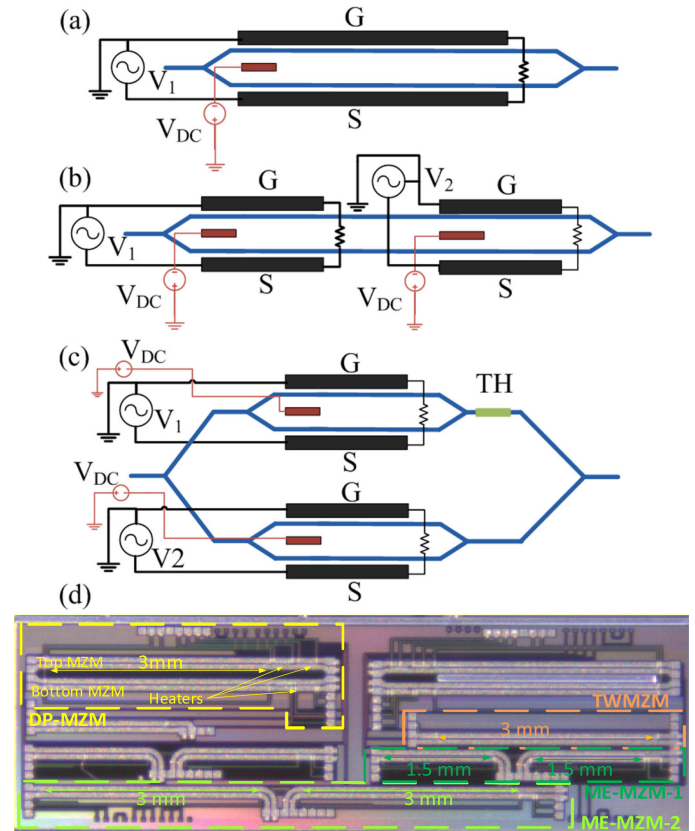

Fig. 1.   (a) Schematic of (a) TWMZM, (b) ME-MZM, (c) DP-MZM and (d) Micrograph of the silicon photonic chip. (TH: Thermo-optic heater).

vertical grating couplers (GCs) are used to couple light in and out of the SiP chip. Back to back insertion loss of the two GCs is measured to be 9.5 dB. A low-loss, compact Y-branch is used as a splitter/combiner to form the interferometer. A resistive thermo-optic heater is used to control the phase and biasing of the modulators. The insertion loss of the TWMZM, DP-MZM, shorter ME-MZM and longer ME-MZM are measured to be 3.3, 4.1, 3.4 and 6.3 dB respectively.

A. PN Junction

All four modulators were fabricated on a silicon-on-insulator (SOI) wafer with a 220-nm thick silicon layer, a 2 μm thick buried oxide layer and a high resistivity 750 Ω-cm silicon substrate in the same multi-project wafer run at IME-A $*$ STAR. Fig. 2 illustrates the cross section of the modulators. Intrinsic regions are inserted periodically with fill factor of 90% along the phase shifter to minimize the current flow in the longitudinal direction (normal to the picture). The phase shifters operate based on the plasma dispersion effect, where the change in the carrier density at the PN junction, caused by the external drive voltages, results in change of the effective index of the waveguides [28].

Table I shows the values for all the dimensions noted in Fig. 2. To reduce optical propagation losses in the waveguides at 1310 nm, the width of the rib waveguides was set at 400 nm which is slightly wider than a strictly single mode waveguide
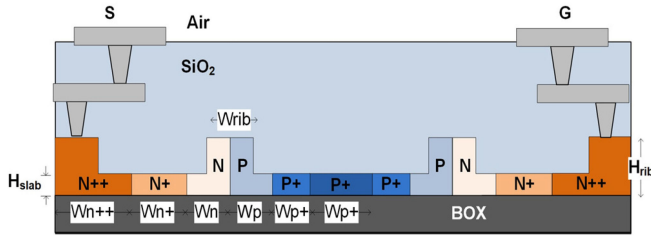
Fig. 2. Cross section of the SiP MZM in series push-pull configuration. (S: Signal, G: Ground).

TABLE I
WAVEGUIDE AND PN JUNCTION DIMENSIONS

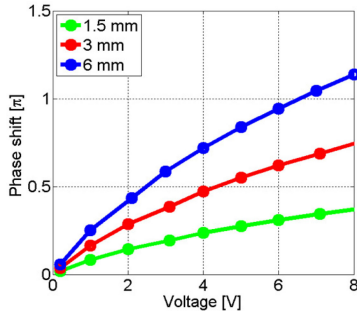| Dimension	Value	Dimension	Value
W_{rib}	0.4 µm	H_{rib}	0.22 µm
W_{n++}	7 µm	H_{slab}	0.09 µm
W_{n+}	0.78 µm	H_{metal}	2 µm
W_n	0.42 µm	L_{pn}	18 µm
W_{P++}	28.6 µm	$L_{intrinsic}$	2 µm
W_{p+}	0.8 µm	Λ	90%
W_p	0.4 µm	H_{BOX}	2 µm

Fig. 3. Phase shift versus voltage of various phase shifter lengths.

with 220 nm height at O band. The two PN junctions are connected in series with opposite polarity, to allow for SPP operation, which effectively lowers the combined capacitance of the two diodes [29].

The highly doped levels (P++ and N++) are used to create ohmic contacts, and the intermediate doping levels (P+ and N+) are used to reduce series resistance of the PN junction and minimize the optical losses due to high concentration of dopants since. The intermediate doping levels have negligible effect on the capacitance of the junctions since the capacitance is created mainly at the junction of P and N. Furthermore, the intermediate doping levels can be used to optimize the microwave losses by adding an extra level of control to the series resistance of the junctions. On the other hand, the change in effective index and loss due to the plasma dispersion effect is dictated by the P and N doping levels due to the optical mode being tightly confined near the waveguide core. The peak concentration of the P and N for this process are 7×10^{17} cm^{-3} and 5×10^{17} cm^{-3} respectively [30]. Fig. 3 shows the measured phase-shift versus applied

voltages for 1.5 mm, 3 mm and 6 mm long phase shifters. The measurements are taken at 1310 nm.

As seen in Fig. 3 the phase shift due to plasma dispersion effect does not increase linearly with applied voltage. This non-linearity is measured to be more pronounced in the O-band compared to the C-band. Furthermore, beyond 8 V reverse bias, the width of the PN junction depletion region does not change drastically, therefore the change in concentration of the carriers which induces change in n$_{eff}$ of the waveguide in very small. Consequently, the phase change is not strong enough beyond 8 V and as a result a full π phase change cannot be achieved with smaller phase shifter lengths. For OOK modulation, this will have no negative consequence on the transmission performance of the modulator; however, for a multi-amplitude modulation format such as PAM-4 this requires further non-linearity compensation to achieve equidistant amplitude levels. This non-linearity is further discussed in the next sections. A resistive heater is used on one arm of each MZM to control the biasing and operating conditions. In the case of the DP-MZM, three heaters are used, one for each inner MZM to apply proper biasing of the modulators and one on the outer MZM to ensure in-phase combination of the two branches.

B. Microwave Characterization

Since we fabricated the modulators in the same process as in [31], the electrode design of the modulators requires minimal update. Three main criteria need to be met in the design of the electrodes to enable the targeted BW. First, the PN junction loaded electrodes should have 50 Ω characteristic impedance, to minimize any RF back reflection. Second, microwave losses must be minimized since the main limiting factor in BW performance of the modulators are RF loss, and finally, the optical group velocity and microwave phase velocity should be closely matched. We follow the same design methodology presented in [31] to optimize the coplanar strip waveguide (CPS) travelling wave electrodes for the O-band modulators and to calculate microwave losses and velocity mismatch limitation. Since the process parameters are the same (i.e., doping density, metal trace material, metal thickness etc.), the conductor and dielectric losses remain the same. It should be noted that the effects of change in the waveguide geometry and doping dimensions on the PN junction capacitance and series resistance versus the C-band case in [31] are minimal and can be neglected. The capacitance of the PN junctions is simulated to be 230 pf/m at 0 V, and 160 pf/m at −3 V which is within 1% of the values for 500 nm wide waveguide used for 1550 nm applications. On the other hand, the group index of the optical TE mode at 1310 nm is simulated to be 3.96, while the microwave effective index of the PN junction loaded electrodes varies from 4 to 3.7 between 1 to 50 GHz. This results in a slightly higher velocity mismatch between the optical group velocity and microwave phase velocity compared to C-band TWMZM. Taking into consideration the changes mentioned above and to maintain 50 Ω characteristic impedance, we arrive at 60 µm electrode width and 35 µm spacing. However due to higher velocity mismatch and
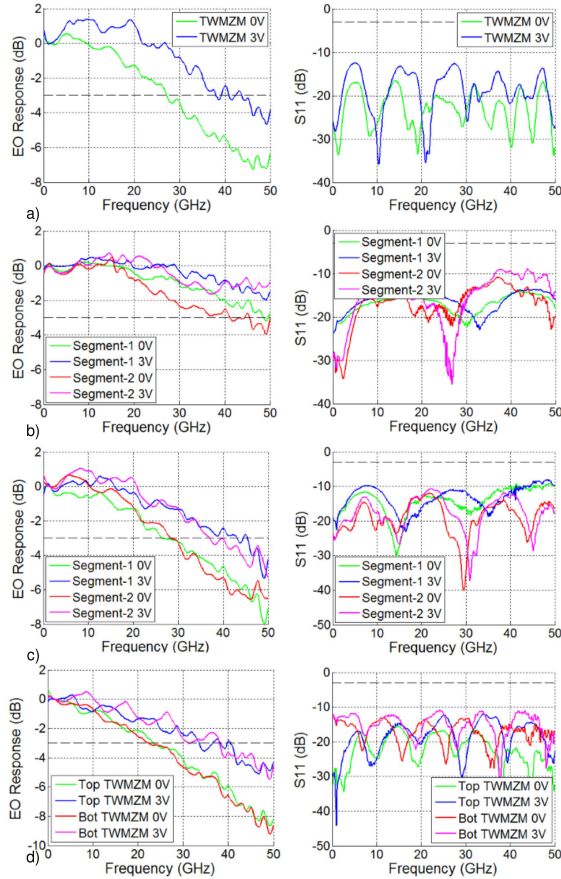
Fig. 4.   EO and S11 response of (a) TWMZM, (b) ME-MZM with 1.5 mm long phase shifter, (c) ME-MZM with 3 mm long phase shifters and, (d) DPZMZM.

considering our required ≥ 35 GHz EO bandwidth, the electrode length must be kept ≤ 4.1 mm. Fig. 4 shows the measured EO S21 and S11 curve of all modulators at 0 V and -3 V reverse bias normalized to 1.5 GHz. The difference between the segments of the ME-MZMs are mainly caused by their difference in lengths. For example, as shown in Fig. 1(d) the second segment of both ME-MZMs are slightly longer than their first segments to accommodate the optical routing to the GCs and also the thermo-optic tuners.

C. Transfer Function and Linearity

MZMs function as optical DACs. For PAM-N they are operated as N-bit DACs. Therefore, similar to electrical DACs, linearity is an important factor of their performance. On one hand a MZM's transfer function is a nonlinear cosine function, on the other hand SiP PN junction phase shifters are also nonlinear. This creates extra challenges for PAM-N modulation using SiP MZMs. In this section we present the measured transfer function of the SiP MZM and characterize their differential nonlinearity (DNL) and integral nonlinearity (INL) [32]. Furthermore, we investigate the ratio of level separation mismatch (R_{LM}) for each modulator. The DNL is defined as the ratio of an actual analog

step to the ideal value of the least-significant bit (LSB).

$$DNL = \left| \frac{I_{N+1} - I_N}{I_{LSB}} - 1 \right| \tag{1}$$

where I_N is the output intensity at level N corresponding to the digital input voltage V_N, and I_{LSB} is the ideal amplitude of the least significant bit. DNL allows us to assess the extinction ratio penalty of each of the four PAM-4 levels. DNL varies between 0 and 1, where 0 is the ideal case. INL, on the other hand is the ratio of an actual measured output intensity to the ideal output.

$$INL = \left| \frac{I_N - I_{zero}}{I_{LSB}} - N \right| \tag{2}$$

It should be noted that INL is defined for the drive voltage operation range not the entire transfer function range. R_{LM} indicates the vertical linearity of the signal and is a measurement for mismatch between PAM-4 levels [33].

$$R_{LM} = \frac{6.S_{\min}}{V_3 - V_0} \tag{3}$$

where S_{min} is half of the swing between adjacent symbols, V_3 and V_0 correspond to the first and fourth PAM-4 levels.

$$S_{\min} = \frac{1}{2}\min\left(V_3 - V_2, V_2 - V_1, V_1 - V_0\right) \tag{4}$$

similarly, V_2 and V_1 correspond to the third and second PAM-4 levels. In an ideal scenario $R_{LM} = 1$, while the 100 GbE PAM-4 specifications require $R_{LM} \geq 0.92$ [34].

To investigate the linearity of each of the presented modulators, we first point out the difference between their transfer function. The transfer function of a conventional MZM is [32]:

$$\frac{I_o}{I_i} = \frac{1}{2}\left[1 + \cos(\theta)\right] \tag{5}$$

where θ is the phase change in radians.

For OOK modulation, a MZM is usually operated at quadrature point to achieve maximum extinction for the transfer of drive voltage to optical power, when the MZM is driven to V_π. For PAM-4 however, if the MZM is driven to V_π, the 4 amplitude levels will not be equidistant, due to sine wave form of the MZM transfer function. To mitigate the non-linearity of MZM, a common practice is to limit the operation voltage of the MZM to the linear part of the transfer function. It should also be noted that reducing the operation range of a transfer function results in overall ER reduction of the PAM-4 levels, hence a careful study of the ER penalty is important in improving the transmission performance of the MZM.

Fig. 5, shows the transfer function of the presented SiP TWMZM using the measured phase-shift presented in Fig. 3 versus a MZM with a linear phase shifter (red curve). As shown in Fig. 3, due to the nonlinearity of the SiP phase shifters, the transfer function of the SiP TWMZM is not a perfect sine wave and therefore is not symmetric with respect to quadrature point ($I_o = 0.5 \times I_i$) where I_o is the optical intensity at the output of the modulator. As a result, to improve the linearity of the SiP TWMZM for PAM-4 operation, in addition to reducing the operation range (i.e., drive voltage), the bias point of the MZM should be adjusted accordingly. Since the shape of the transfer
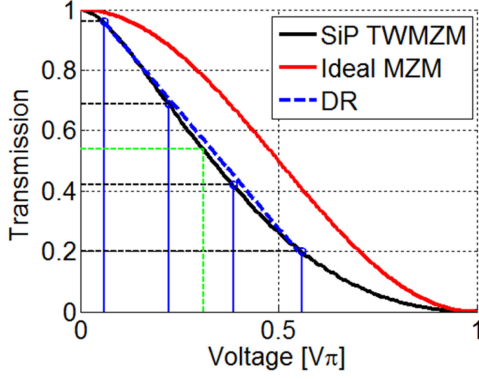
Fig. 5. Transmission spectrum of SiP TWMZM and a MZM with linear phase shifters. (DR: Dynamic Range). Dashed green line identifies the bias point at $0.55 \times I_i$.

function is dependent on the PN junction, the bias point of the presented MZMs is empirically found to be at $I_o = 0.54 \times I_i$, slightly higher than the quadrature point. For example, as shown in Fig. 5 if the SiP MZM is operated at quadrature point ($I_o = 0.5 \times I_i$) and driven by $0.5 \times V_\pi$, the DNL and INL are 0.23 and 0.21 respectively. However, by changing the operation point to $I_o = 0.55 \times I_i$ (shown as green dashed line) the DNL and INL are reduced to 0.13 and 0.12. This significantly improves the BER performance of the system in which the SiP MZM is used. From Fig. 5, it can be observed that reducing the driving range (DR) of the modulator to $0.5 \times V_\pi$ only reduces the transmission range to $0.76 \times I_i$ instead of I_i, and as a result the four intensity levels of PAM-4 are 0.96, 0.69, 0.42 and 0.2 and the R_{LM} is 0.87, while if the modulator is driven by V_π and bias at quadrature the intensity levels are 1, 0.63, 0.05 and 0. It is clear that in this condition the two lowest intensity levels are very close, while the two middle levels are far apart. This reduction in transmission range can result in up to 1 dB ER reduction. Due to their high V_π, SiP MZMs are often driven with fraction of their V_π [36], for example in [37] a 50 Gb/s OOK error free modulation is achieved by driving the modulator to 12% of the measured V_π. In the next sections we experimentally evaluate the effects of reducing the driving voltage on the transmission performance of the presented modulators.

The transfer function of ME-MZM differs from that of single electrode MZM. A ME-MZM operates by summing the phase-shift of each segment to create the PAM levels, while a DP-MZM operates by summing the output intensity of each child MZM. The transfer function of ME-MZM ignoring losses, can be written as:

$$\frac{I_o}{I_i} = \frac{1}{2} \left[1 + \cos(\theta_1 + \theta_2) \right] \qquad (6)$$

where, θ_1 and θ_2 are the phase changes from modulating each segment. Fig. 6 shows the transmission of ME-MZM as a function of the drive voltages of the two segments. The red dot indicates the biasing point of the device, and the black dots indicate the 4 intensity levels of PAM-4 adjusted such to compensate for the non-linear transfer function of the device. The four intensity levels of the longer ME-MZM are 0.94, 0.7, 0.4 and 0.16 while the PAM-4 intensity levels for the shorter ME-MZM are 0.89,
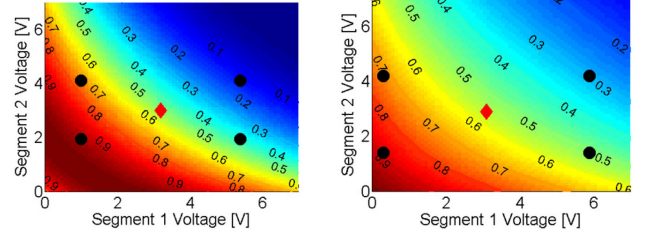

Fig. 6. (a) The transmission spectrum of ME-MZM with 3 mm phase shifters, and (b) transmission spectrum of ME-MZM with 1.5 mm phase shifters as function of the drive voltages of the two segments. The black circles on the graphs mark the PAM-4 levels, and the red diamond shows the bias point of the modulators.
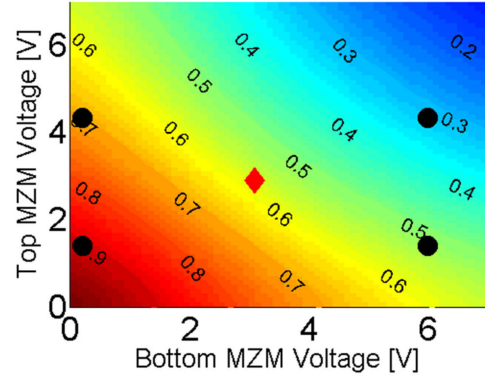

Fig. 7. Transmission spectrum of DP-MZM as a function of the drive voltage of top and bottom inner MZMs.

0.71, 0.5 and 0.3 respectively. the R_{LM} values of the longer and shorter ME-MZM are 0.92, and 0.915 respectively. The ME-MZM with 3 mm long segments has a more linear transmission function than the ME-MZM with 1.5 mm long phase shifters. As a result, the DNL and INL of the longer ME-MZM are 0.05 and 0.07 for the transmission range of $0.8\,I_i$, while the DNL and INL of the shorter ME-MZM are 0.07 and 0.09 for the transmission range of $0.6\,I_i$. Similarly, from Similarly, the transfer function of the DP-MZM when both arms of the outer MZM are in phase, can be written as:

$$\frac{I_o}{I_i} = \frac{1}{2} \left[\frac{1}{2} \left[1 + \cos(\theta'_1) \right] + \frac{1}{2} \left[1 + \cos(\theta'_2) \right] \right] \qquad (7)$$

where θ'_1 and θ'_2 are the phase changes from the top inner MZM and bottom inner MZM, respectively. Fig. 7 shows the transfer function of DP-MZM as a function of the two drive voltages of inner MZMs. From the curvature of the graph, it can be seen that DP-MZM has a more linear transmission than the TWMZM or the shorter ME-MZM even though it has the same V_π value. This can be explained by looking at the driving range of the inner MZMs. The inner MZMs are driven by a smaller fraction of their V_π, compared to the ME-MZM and TWMZM; hence they are operating in a more linear regime. Also, as shown in (7), the output intensity of the DP-MZM is the sum of the output of both inner MZMs, and summation is a linear operation, hence the DP-MZM is expected to have a more linear transmission compared to a ME-MZMs with the same phase shifter length.

The red dot on Fig. 7 indicates the bias point of the device where the intensity is close to 0.57, slightly above the quadrature point of the device. The four black dots, indicate the four intensity levels of PAM-4, at 0.31, 0.51, 0.7 and 0.9 of I_i. The calculated DNL and INL for of the DP-MZM are 0.05 while the R_{LM} is 0.966.

Several figures of merit (FOM) have been recently presented in literature for depletion type silicon modulators [38], [39]. These FOMs consider several parameters and can be used for detailed design optimization of modulators for target specifications. However, for general performance assessment, we use a simple FOM, BW/ V_π which has traditionally been used to evaluate the overall expected performance of the modulators compared to each other, where BW is the 3 dB electro-optic bandwidth of the modulator. Modulators with higher FOM are expected to perform better, since a large BW allows the modulator to achieve higher baudrate while lower V_π indicates more efficient phase shifter. From the analysis and characterization of the modulators in this section, the calculated FOM for the TWMZM, DP-MZM, shorter ME-MZM and longer MEMZM are 3, 2.9, 3.7 and 5.4 GHz/V, respectively. The improved FOM of the ME-MZMs are the result of their segmented electrode design. Using multiple electrodes, results in shorter segment lengths and ultimately lower microwave losses, allowing the ME-MZM to have higher BW for longer phase shifter lengths. The shorter ME-MZM has the same total phase shifter length as the TWMZM and the DP-MZM, while its electrodes are shorter, resulting in same V_π as the TWMZM and DP-MZM but significantly higher BW. On the other hand, the longer ME-MZM has similar electrode length as the TWMZM and ME-MZM but with twice the phase shifter length, resulting in similar BW but lower V_π.

III. TRANSMISSION EXPERIMENT

In this section we investigate the transmission performance of each device for OOK and PAM-4 modulation. First, we present the transmission performance of the modulators without using digital signal processing (DSP). For OOK modulation we use a bit pattern generator (BPG) to drive the modulators and a bit error rate tester (BERT) for BER measurements. For PAM-4, we use a 63 GHz real-time oscilloscope (RTO) to capture the received data, as the BERT is not capable of PAM-4 error measurements. Next, we repeat the experiment by replacing the BPG with an 8-bit electrical DAC operating at 88 Gsample/s and apply DSP to the modulator's drive signal. Fig. 8 illustrates the experimental setup for each modulator.

A. Transmission Without DSP

As shown in Fig. 8 the electrical driving signal is generated using a BPG and is then amplified using a 45 GHz radio frequency (RF) amplifier. In the case of TWMZM the amplified signal is directly applied to the modulator using a 50 GHz RF probe. For the DP-MZM and ME-MZM, the delay and skew settings of the BPG along with RF tunable delay lines (TDL) are used to time align two BPG channels before applying them to the modulators through the RF probes. All four modulators are biased at −3 V.
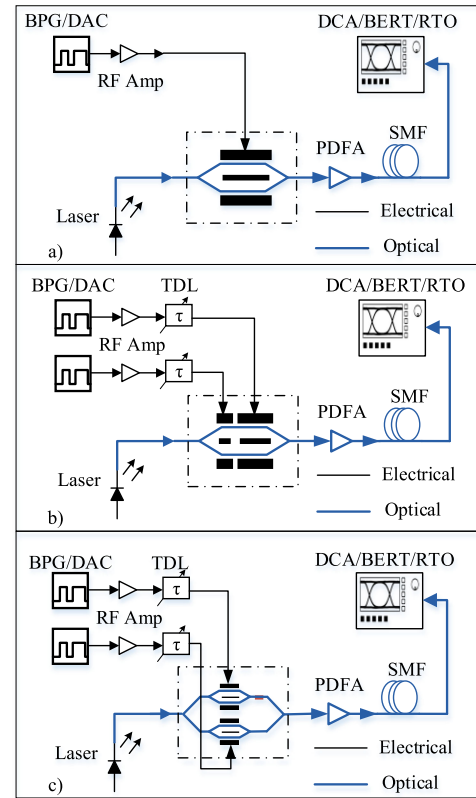

Fig. 8. The experimental setup of (a) TWMZM, (b) ME-MZM, and (c) DP-MZM.

For ME-MZM, the time delay for the drive signal of the second segment can be estimated by dividing the sum of the length of the first segment and the separation between the two segments by the optical group velocity. For DP-MZM, both drive signal path lengths should be the same, and this is achieved by using matched RF cables, and matched RF amplifiers. The TDLs are then used to fine tune the two signal streams. A 13 dBm tunable O-band laser is used as a source for the modulators. Considering the insertion loss from the input GC, and the routing losses, the input power to all three modulators are estimated to be 8 dBm +/− 0.5 dbm. The output modulated signal is then amplified to 5 dBm using a praseodymium-doped fiber amplifier (PDFA) and propagated through various lengths of fiber. The PDFA is used to compensate for the high insertion loss of the grating couplers, and routing losses. In addition, using a transimpedance amplifier (TIA) with the photodetector (PD) can significantly improve receiver sensitivity and reduce the optical power needed at the PD. Fig. 9 demonstrates the 40 Gbaud OOK optical eye diagrams of the modulators driven by 3 V_{PP} drive signals. The presented eyes are captured using the 80 GHz optical sampling head of the digital sampling oscilloscope (DSO). From Fig. 9 it can be seen that both ME-MZM modulators achieve higher extinction compared to TWMZM and DP-MZM. This can be attributed to the lower microwave loss of the shorter ME-MZM and the longer phase-shifter length (lower $V\pi$) in the case of longer ME-MZM. It should however be noted that the ME-MZMs and DP-MZMs
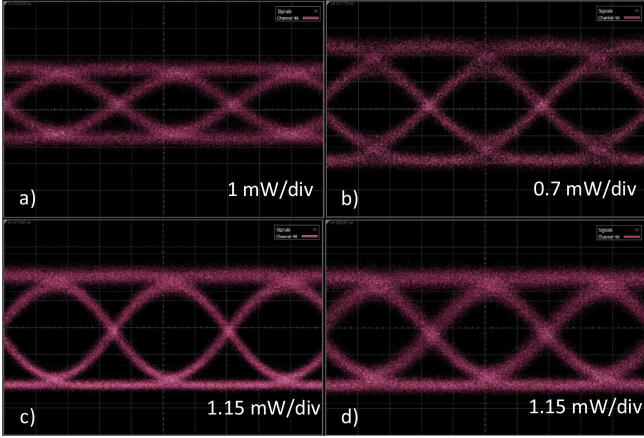
Fig. 9. 40 Gbaud OOK eye diagram of (a) TWMZM, (b) DP-MZM, (c) ME-MZM with 1.5 mm segments, and (d) ME-MZM with 3 mm segments.
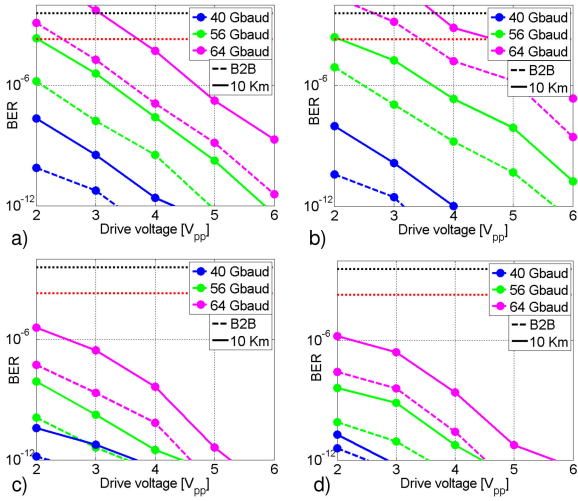

Fig. 10. BER measurements of (a) TWMZM, (b) DPMZM, (c) ME-MZM with 1.5 mm segments and (d) ME-MZM with 3 mm segments.

are operated with two drive signals which increases complexity versus TWMZM.

For OOK modulation, two identical pseudorandom binary sequence (PRBS) signals with the same V_{pp} are applied to both ME-MZM segments and DP-MZM's, child MZMs. A 50 GHz, 0.65 A/W photodetector (PD) is connected to the BERT to receive the signal and measure the BER. The PD did not have a following transimpedance amplifier (TIA). In a practical setting, the linearity of the TIA would play an important role in the performance of the system. Fig. 10 illustrates the BER measurement of each modulator for various baud rates and drive signal voltages in the back-to-back (B2B) and over 10 km of standard single mode fiber (SMF). The dotted horizontal red and black lines indicate the KP4-FEC threshold at 2.4×10^{-4} and HD-FEC threshold at 3.8×10^{-3}.

As expected from the BW/$V\pi$ values presented in previous section, the ME-MZMs perform noticeably better compared to the TWMZM, and DPMZM. It should also be noted that in the case of the shorter ME-MZM, the system is not bandwidth limited, however due to the high $V\pi$ values, the improvement
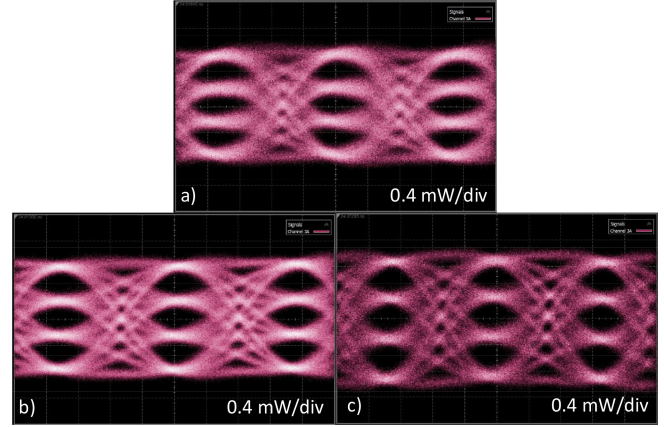

Fig. 11. 40 Gbaud PAM-4 eye diagrams of (a) DP-MZM, (b) shorter ME-MZM, and (c) longer ME-MZM.

in performance is not significant compared to the longer ME-MZM. DP-MZM's inferior performance can be attributed to two factors, first the slightly lower FOM value of the device compared to the other three modulators, and second, the drift of the biasing heaters.

To achieve PAM-4 modulation using DP-MZM and ME-MZM two independent OOK PRBS signals are applied to the modulators as shown in Fig. 8(b-c). Since the BERT used in the experiment is not capable of PAM-4 error counting, we perform the error counting offline, by capturing the received signal using a real-time oscilloscope (RTO). No DSP or equalization is used on the receiver side. Additionally, as our BPG can only transmit OOK signals the TWMZM can't be used to achieve PAM-4 without the use of DSP. Fig. 11 shows the 40 Gbaud PAM-4 eye diagrams of modulators captured using the DSO. The presented eyes are captured using the drive conditions presented in Figs. 6 and 7. For the longer ME-MZM the modulator is biased at 3.2 V and the two drive voltages are 4.4 V and 2.1 V. For shorter ME-MZM the bias voltage is set at 3.0 V and the drive voltages are 5.7 V and 2.7 V. Similarly, for the DP-MZM, the bias voltages of both inner MZMs are set at 3.0 V and the drive voltages are 5.8 V and 3 V.

The longer ME-MZM achieves a higher extinction ratio compared to the other two modulators while driven by lower amplitude drive signals, thanks to its longer phase shifter length. Fig. 12 shows the BER performance of each modulator for various baudrates and drive voltages in the B2B and 10 km transmission. All three modulators are capable of generating 56 Gbaud PAM-4 signals without the use of DSP. However, from Fig. 12 several important observations can be made. The shorter ME-MZM achieves below FEC transmission up to 64 Gbaud. This superior performance can be attributed to the higher BW of this modulator. On the other hand, the BER performance of the shorter ME-MZM is more sensitive to drive voltages compared to the longer ME-MZM. From Fig. 12(b) it can be observed that lowering the drive voltage affects the BER performance of shorter ME-MZM more severely than the longer ME-MZM. This is due to the larger V_π value of the shorter ME-MZM. On the other hand, maximizing the drive voltage
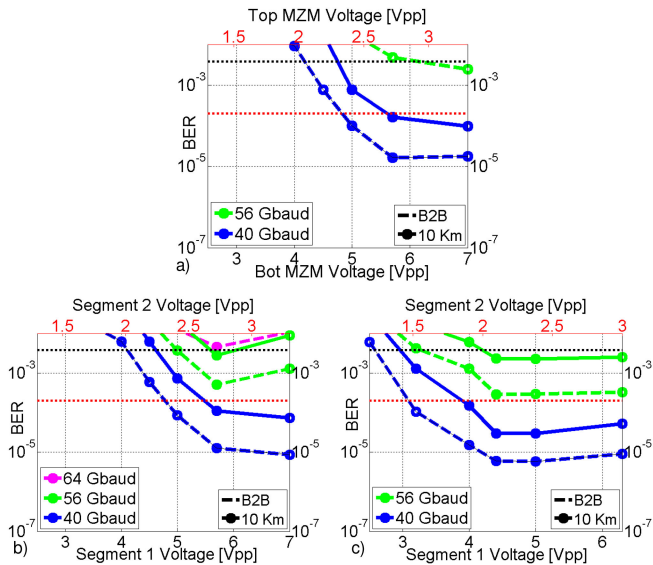
Fig. 12. PAM-4 BER performance of (a) DP-MZM, (b) shorter ME-MZM and (c) longer ME-MZM. The dotted horizontal red and black lines indicate the KP4 forward error correction (FEC) threshold at 2.4×10^{-4} and hard decision (HD) FEC threshold at 3.8×10^{-3} respectively.

Fig. 13. PAM-4 BER performance of the (a) TWMZM, (b) DP-MZM, (c) shorter ME-MZM, and d) longer ME-MZM. The dashed horizontal redlines indicate the KP4 FEC threshold at 2.4×10^{-4} and HD-FEC threshold at 3.8×10^{-3}.

($7\,V_{pp}$ and $3.3\,V_{pp}$), negatively impacts the BER performance at 56 Gbaud and 64 Gbaud. This can be explained by referring to the linearity discussion in the previous section and in Fig. 6(a). By increasing the drive voltages, the modulator suffers more from the non-linearity of its transfer function, resulting in PAM-4 amplitude levels that are not equidistant which in turn results in higher error counts. Using both of the ME-MZMs, we achieve 10 km transmission at 56 Gbaud below HD FEC threshold, which is highest baud rate achieved using an O-band SiP modulator.

The longer ME-MZM can achieve below FEC transmission while driven by lower drive voltages, compared to the other two modulators due to its longer phase shifter length. Like the other two modulators at higher drive voltages, the BER performance deteriorates slightly because of nonlinearity.

B. Transmission With DSP

DSP is widely used in long haul communication systems, while for short reach communication the use of DSP is still a topic of debate. However, in recent years and because of the growing bandwidth demand and adaptation of PAM-4 for 400 Gb/s systems, DSP is viewed as a necessary enabler of higher modulation formats, and higher baudrates. In this section we investigate the improvements achieved using DSP.

To quantitatively assess the improvements achieved by applying DSP, we replace the BPG with an 8-bit, 88 GSample/s electrical DAC, while the rest of the experimental setup remains the same. We use the same transmitter DSP presented in detail in [40] which includes raised cosine pulse shaping, RF pre-emphasis up to the output of the RF amplifiers, and quantization. For the case of PAM-4 modulation using TWMZM, the PAM-4 signal is generated in the electrical domain using the
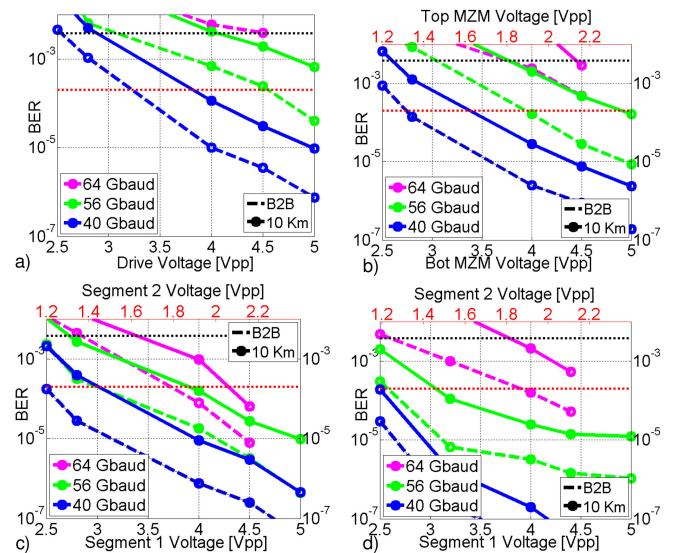
DAC. PAM-4 amplitude levels are adjusted using the DAC to compensate for the TWMZMs non-linearity. For the DP-MZM and ME-MZM cases the modulators are driven by OOK signals. On the receiver side, we use the RTO to capture the modulated signal and perform offline signal processing which consists of: sampling the received signal at 160 GSample/s, matched filtering, clock recovery, receiver equalization and symbol decision. Fig. 13 demonstrates the BER performance of the modulators for various drive voltages and symbol rates.

From Fig. 13 it is clear that DSP significantly improves the BER performance of the system. More specifically at higher symbol rate the effect of equalization is more noticeable, where significant improvements can be observed at 64 Gbaud. It should be noted that due to stronger equalization at 64 Gbaud the maximum achievable peak-to-peak voltage is $4.5\,V_{pp}$. Both ME-MZMs can be used for 64 Gbaud PAM-4 generation below the KP-4 FEC. Since we are operating close to 1310 nm, the effects of dispersion are minimal and we are limited mostly by the optical fiber losses. In addition, it is observed that DP-MZM and ME-MZMs provide a substantial improvement over TWMZM. As mentioned previously the TWMZM requires an electrical PAM-4 signal, however the DP-MZM and ME-MZMs are operated using OOK electrical signals. The superior SNR and ER of the OOK electrical signal has a clear effect on the performance of these devices.

Use of DSP in a commercial TOSA/ROSA results in considerable increase in power consumption. Similarly requiring two drive voltages to operate DP-MZM and ME-MZMs increases the power consumption. To impartially assess the overall performance of each modulator a thorough analysis of modulator and drive circuitry power consumption is required. However, calculating the DAC or the BPG's power consumption is not possible. Hence, we estimate the power consumed only by the modulator. The power consumed by each modulator can be

TABLE II
MINIMUM POWER CONSUMPTION OF EACH MODULATOR FOR BELOW HD FEC PAM-4

PAM-4 Baud [Gbaud]	TWMZM		DP-MZM		ME-MZM (1.5 mm segments)		ME-MZM (3 mm segments)	
	V_{rms} [V]	Power (pj/bit)	V_{rms1}, V_{rms2} [V]	Power (pj/bit)	V_{rms1}, V_{rms2} [V]	Power (pj/bit)	V_{rms1}, V_{rms2} [V]	Power (pj/bit)
40, Without DSP	NA	NA	1.4, 0.7	0.63	1.6, 0.7	0.78	1.1, 0.5	0.39
40, With DSP	1.0	0.25	0.9, 0.4	0.24	0.9, 0.4	0.24	0.9, 0.4	0.24
56, Without DSP	NA	NA	2.5, 1.2	1.13	2.0, 1.0	0.89	1.4, 0.7	0.44
56, With DSP	1.4	0.36	1.4, 0.7	0.44	1, 0.5	0.21	0.9, 0.4	0.17
64, Without DSP	NA	NA	NA	NA	NA	NA	NA	NA
64, With DSP	NA	NA	1.6, 0.8	0.49	1.4, 0.7	0.38	1.1, 0.3	0.25

The $V_{i,rms}$ values are calculated from the drive voltages shown in Figs. 12 and 13.

estimated by $P = \sum_{i=1}^{N} \frac{V_{i,RMS}^2}{R}$, where, N is the number of drive signal and $V_{i,rms}$ is the root-mean-square of the ith drive voltage [23]. Table II shows the minimum power consumption of each modulator to achieve sub HD FEC transmission at various symbol rates. Use of DSP lowers the BER of the modulators as expected, however this effect is more noticeable in the DP-MZM and longer ME-MZM where the modulators are BW limited for high symbol rates. At 56 Gbaud, which is the target symbol rate per lambda for 400 Gb/s systems, the longer ME-MZM is clearly the optimized design, where without the use of DSP, the modulator achieves the lowest power consumption. However, DSP enables the modulator to achieve transmission below KP-4 FEC at 56 Gbaud.

IV. CONCLUSION

In this manuscript, we investigate different Mach-Zehnder interferometer-based O-band modulators for 400 Gb/s short reach transmission system employing PAM-4 modulation. We present modulators designs and study their transfer function and linearity in detail. We present ideal biasing points and driving conditions for each modulator based on their phase shifter length and transfer function. A simple figure of merit, in the form of BW/V_π, is used to assess the overall performance of the modulators. We present an optimized design in the form of 2 segments ME-MZM with 3 mm long phase shifters and experimentally show that this modulator provides a clear improvement in transmission system performance compared to the other presented modulators. Additionally, we show that generating PAM-4 signal in optical domain using modified MZM structures such as ME-MZM and DP-MZM could result in better transmission performance compared to using traditional single electrode TWMZM. It should be noted that while ME-MZMs could provide higher 3-dB BW for a comparable Vπ value as TWMZM, the optical loss of the ME-MZM would be higher. This could affect the over performance of the transmission system depending on the optical loss budget, and hence would require further optimization The BER measurements presented,

have been performed in a research lab setting, to further quantify the effects of loss on the performance of the modulators and for practical implementations, more detailed studies such as BER vs. optical modulation amplitude (OMA) should be performed. Furthermore, IEEE 400G ethernet standard introduces transmitter dispersion eye closure (TDECQ) as an important metric for performance of 400 G transceiver. However, we were unable to perform these measurements in our lab. The study presented here, focuses mainly on the modulator structure, it should be noted that for practical implementations of transceiver, the receiver components, and loss budget of transmitter play a significant role in the performance of the system. Finally, we achieve the highest sub HD FEC threshold symbol rate presented for an O-band SiP modulator without DSP.

REFERENCES

[1] IEEE P802.3ba 40 Gb/s and 100 Gb/s Ethernet Task Force. Jun. 2010. [Online]. Available: http://www.ieee802.org/3/ba/

[2] K. Zhong *et al.*, "Experimental study of PAM-4, CAP-16, and DMT for 100 Gb/s short reach optical transmission systems," *Opt. Express*, vol. 23, no. 2, pp. 1176–1189, 2015.

[3] P. Dong, X. Liu, S. Chandrasekhar, L. L. Buhl, R. Aroca, and Y. K. Chen, "Monolithic silicon photonic integrated circuits for compact 100 Gb/s coherent optical receivers and transmitters," *IEEE J. Sel. Topics Quantum Electron.*, vol. 20, no. 4, pp. 150–157, Jul./Aug. 2014.

[4] J. Lin, H. Sepehrian, L. A. Rusch, and W. Shi, "CMOS-compatible silicon photonic IQ modulator for 84 gbaud 16QAM and 70 gbaud 32QAM," in *Proc. Opt. Fiber Commun. Conf. Expo.*, San Diego, CA, USA, 2018, Paper Tu2E.4.

[5] L. Chen *et al.*, "Silicon photonics for 100G-and-beyond coherent transmissions," in *Proc. Opt. Fiber Commun. Conf.*, Anaheim, CA, USA, 2016, Paper. Th1B.1.

[6] "100 GLambda multi source agreement," 400G-FR4 Technical Spec D2p0, Rev2, Sep. 18, 2018.

[7] J. Zhou, C. Yu, and H. Kim, "Transmission performance of OOK and 4-PAM signals using directly modulated 1.5-μm VCSEL for optical access network," *J. Lightw. Technol.*, vol. 33, no. 15, pp. 3243–3249, Aug. 2015.

[8] C. Xie *et al.*, "400-Gb/s PDM-4PAM WDM system using a monolithic 2×4 VCSEL array and coherent detection," *J. Lightw. Technol.*, vol. 33, no. 3, pp. 670–677, Feb. 2015.

[9] A. Roshan-Zamir *et al.*, "A two-segmented optical DAC 40 Gb/s PAM4 silicon microring resonator modulator transmitter in 65nm CMOS," in *Proc. IEEE Opt. Interconnects Conf.*, May 2017, pp. 5–6.

[10] R. Li *et al.*, "Silicon photonic ring-assisted MZI for 50 Gb/s DAC-less and DSP-free PAM-4 transmission," *IEEE Photon. Technol. Lett.*, vol. 29, no. 12, pp. 1046–1049, Jun. 2017.

[11] J. Sun *et al.*, "A 128 Gb/s PAM4 silicon microring modulator," in *Proc. Opt. Fiber Commun. Conf. Postdeadline Papers*, San Diego, CA, USA, 2018, Paper Th4A.7.

[12] R. Li *et al.*, "High-speed low-chirp PAM-4 transmission based on push-pull silicon photonic microring modulators," *Opt. Express*, vol. 25, no. 12, pp. 13222–13229, 2017.

[13] R. Dubé-Demers, S. LaRochelle, and W. Shi, "Low-power DAC-less PAM-4 transmitter using a cascaded microring modulator," *Opt. Lett.*, vol. 41, no. 22, pp. 5369–5372, 2016.

[14] N. Abadía *et al.*, "Low-power consumption Franz-Keldysh effect plasmonic modulator," *Opt. Express*, vol. 22, no. 9, pp. 11236–11243, 2014.

[15] J. Verbist *et al.*, "DAC-less and DSP-free 112 Gb/s PAM-4 transmitter using two parallel electroabsorption modulators," *J. Lightw. Technol.*, vol. 36, no. 5, pp. 1281–1286, Mar. 2018.

[16] A. Abbasi *et al.*, "III–V-on-silicon C-band high-speed electro-absorption-modulated DFB laser," *J. Lightw. Technol.*, vol. 36, no. 2, pp. 252–257, Jan. 2018.

[17] H. Zwickel *et al.*, "Silicon-organic hybrid (SOH) modulators for intensity-modulation / direct-detection links with line rates of up to 120 Gbit/s," *Opt. Express*, vol. 25, pp. 23784–23800, 2017.

[18] M. Li, L. Wang, X. Li, X. Xiao, and S. Yu, "Silicon intensity Mach–Zehnder modulator for single lane 100 Gb/s applications," *Photon. Res.*, vol. 6, no. 2, pp. 109–116, 2018.

[19] S. Shao *et al.*, "Optical PAM-4 signal generation using a silicon Mach-Zehnder optical modulator," *Opt. Express*, vol. 25, no. 19, pp. 23003–23013, 2017.

[20] H. Sepehrian, A. Yekani, L. A. Rusch, and W. Shi, "CMOS-photonics codesign of an integrated DAC-Less PAM-4 silicon photonic transmitter," *IEEE Trans. Circuits Syst. I, Reg. Papers*, vol. 63, no. 12, pp. 2158–2168, Dec. 2016.

[21] A. Samani, V. Veerasubramanian, E. El-Fiky, D. Patel, and D. V. Plant, "A silicon photonic PAM-4 modulator based on dual-parallel Mach-Zehnder interferometers," *IEEE Photon. J.*, vol. 8, no. 1, Feb. 2016, Art. no. 7800610.

[22] A. Samani *et al.*, "Ook and pam optical modulation using a single drive push pull silicon Mach-Zehnder modulator" in *Proc. Int. Conf. Group IV Photon.*, Paris, France, 2014, pp. 45–46.

[23] A. Samani *et al.*, "Experimental parametric study of 128 Gb/s PAM-4 transmission system using a multi-electrode silicon photonic Mach Zehnder modulator," *Opt. Express*, vol. 25, no. 12, pp. 13252–13262, 2017.

[24] A. Samani *et al.*, "Silicon photonics modulator architectures for multi-level signal generation and transmission," in *Proc. Opt. Fiber Commun. Conf.*, Los Angeles, CA, USA, 2017, Paper Tu2H.4.

[25] M. Papuchon, C. Puech, and A. Schnapper, "4-bits digitally driven integrated amplitude modulator for data processing," *Electron. Lett.*, vol. 16, no. 4, pp. 142–144, Feb. 14, 1980.

[26] A. Yacoubian and P. K. Das, "Digital-to-analog conversion using electrooptic modulators," *IEEE Photon. Technol. Lett.*, vol. 15, no. 1, pp. 117–119, Jan. 2003.

[27] P. Dong, L. Chen, and Y. Chen, "High-speed low-voltage single-drive push–pull silicon Mach–Zehnder modulators," *Opt. Express*, vol. 20, no. 6, pp. 6163–6169, Mar. 2012.

[28] R. Soref and B. Bennett, "Electrooptical effects in silicon," *IEEE J. Quantum Electron.*, vol. QE-23, no. 1, pp. 123–129, Jan. 1987.

[29] D. Patel *et al.*, "Design, analysis, and transmission system performance of a 41 GHz silicon photonic modulator," *Opt. Express*, vol. 23, no. 11, pp. 14263–14287, 2015.

[30] M. Streshinsky *et al.*, "Low power 50 Gb/s silicon traveling wave Mach–Zehnder modulator near 1300 nm," *Opt. Express*, vol. 21, no. 25, pp. 30350–30357, 2013.

[31] A. Samani *et al.*, "A low-voltage 35-GHz silicon photonic modulator-enabled 112-Gb/s transmission system," *IEEE Photon. J.*, vol. 7, no. 3, Jun. 2015, Art. no. 7901413.

[32] 16. Y. Ehrlichman, O. Amrani, and S. Ruschin, "Improved digital-to-analog conversion using multi-electrode Mach-Zehnder interferometer," *J. Lightw. Technol.*, vol. 26, no. 21, pp. 3567–3575, Nov. 2008.

[33] PAM4 Signaling in High Speed Serial Technology: Test, Analysis, and Debug, Application Note, Techtronix. 2016. [Online]. Available: www.tek.com/application/100g-optical-electrical-tx-rx

[34] IEEE Standard for Ethernet, IEEE Std 802.3, Amendment 10, 2017.

[35] G. Agrawal, *Fiber-Optic Communication Systems*. Hoboken, NJ, USA: Wiley, 2013.

[36] Z. Yong *et al.*, "RF and thermal considerations of a flip-chip integrated 40+ Gb/s silicon photonic electro-optic transmitter," *J. Lightw. Technol.*, vol. 36, no. 2, pp. 245–251, Jan. 2018.

[37] T. Baehr-Jones *et al.*, "Ultralow drive voltage silicon traveling-wave modulator," *Opt. Express*, vol. 20, no. 11, pp. 12014–12020, 2012.

[38] D. Gill, C. Xiong, J. Rosenberg, P. Pepeljugoski, J. Orcutt, and W. Green, "Modulator figure of merit for short reach data links," *Opt. Express*, vol. 25, no. 20, pp. 24326–24339, 2017.

[39] H. Sepehrian, A. Yekani, W. Shi, and L. Rusch, "Assessing performance of silicon photonic modulators for pulse amplitude modulation," *IEEE J. Sel. Topics Quantum Electron.*, vol. 24, no. 6, pp. 1–10, Nov./Dec. 2018.

[40] E. El-Fiky, M. Chagnon, M. Sowailem, A. Samani, M. Morsy-Osman, and D. V. Plant, "168-Gb/s single carrier PAM4 transmission for intra-data center optical interconnects," *IEEE Photon. Technol. Lett.*, vol. 29, no. 3, pp. 314–317, Feb. 1, 2017.

Alireza Samani received the B.A.Sc. degree in electrical engineering from the University of Waterloo, Waterloo, ON, Canada, in 2012, and the M.Eng. and Ph.D. degrees in electrical engineering from the McGill University, Montreal, QC, Canada, in 2015 and 2019, respectively. He has authored or coauthored more than 40 journal and conference papers. He is currently working on integrated photonics for quantum computing applications with the Quantum Matter Institute, Vancouver, BC, Canada. His research interests include high-speed silicon photonic devices for optical interconnects and quantum communications. He has received NSERC CREATE SiEPIC-Scholarship, NSERC postgraduate doctoral scholarship, Fonds de Recherche du Québec - Nature et Technologies Doctoral Award, SPIE Optics and Photonics Education Scholarship and McGill Engineering Doctoral Award during his Ph.D. studies. In 2018. he was awarded the prestigious Steward Blusson Quantum Matter Institute Postdoctoral Fellowship.

Eslam El-Fiky received the M.Sc. and B.Sc. degrees from Alexandria University, Alexandria, Egypt, in 2014 and 2010, respectively. He is currently working toward the Ph.D. degree at the Photonic Systems Group, McGill University, Montreal, QC, Canada. He has published more than 65 journal and conference papers. His current research interests include silicon photonic devices and circuits, digital signal processing for high-speed long-haul and short-reach optical communications, and passive optical networks.

Mohamed Morsy-Osman received the B.S. and M.S. degrees from Alexandria University, Alexandria, Egypt, in 2006 and 2009, respectively, and the Ph.D. degree from McGill University, Montreal, QC, Canada, in 2015. Since 2015, he has been with the Electrical Engineering Department, Alexandria University, where he is currently an Assistant Professor. He is currently a Visiting Professor with the Electrical and Computer Engineering Department, McGill University, where he has previously held different positions as a Research Assistant and a Postdoctoral Fellow. He has published more than 100 journal and conference papers. His current research interests include digital signal processing (DSP) for high-speed transport, access and short-reach optical communications. Also, his interests span optical burst switched networks (OBSNs), optical code-division multiple-access (OCDMA) networks, media access control (MAC) protocols in optical networks. He is the recipient of both the 2014 IEEE Photonics Society Best Graduate Student Fellowship and the 2014 SPIE Graduate Scholarship in Optics and Photonics.

Rui Li received the B.Eng. degree in optical engineering from Zhejiang University, Hangzhou, China, in 2013, and the Ph.D. degree from McGill University, Montréal, QC, Canada, in 2018. She is currently a Research Engineer with Huawei, Shenzhen, China. She has authored and coauthored more than 20 journal and conference papers. Her research interests include high-speed optical transmission systems based on silicon photonic devices. She has received NSERC CREATE SiEPIC scholarship, PERSWADE award, and Li & Fung scholarship.

David Patel, biography not available at the time of publication.

Thang Hoang received the bachelor's degree in electrical engineering, the master's degree in electrical engineering from the Catholic University of America, Washington, DC, USA, in 2010 and 2011, respectively, and the Ph.D. degree in electrical engineering from McGill University, Montréal, QC, Canada, in 2018. He is currently working with ADVA Optical Networking, Ottawa, ON, Canada as an R&D Engineer. His research interests include, but not limited to, optical transceivers for data center applications, integrated photonics, and 5G access networks. He has authored/coauthored more than 40 peer-reviewed journals and conference proceedings, including two invited papers and one top-scored proceeding. He received the SPIE Graduate Scholarship in Optics and Photonics in 2014, CMC TexPo Huawei Industrial Collaboration Award 2016, and IEEE Photonics Graduate Fellowship 2018.

Maxime Jacques, biography not available at the time of publication.

Mathieu Chagnon received the Ph.D. degree from the Department of Electrical and Computer Engineering in the Photonics Systems Group, McGill University, Montréal, QC, Canada, in 2016, during which he was awarded the IEEE Photonics Society Graduate Student Fellowship, the SPIE Optics and Photonics Education Scholarship, and the Alexander Graham Bell Canada Graduate Scholarship. He conducted his postdoc with the University of Stuttgart, Germany, for which he was awarded the prestigious Postdoctoral Fellowships from the Natural Sciences and Engineering Research Council of Canada. He made seminal contributions in the field of short-reach direct-detect systems, most notably on multidimensional self-beating formats, transceivers and signal processing. He co-authored a book chapter on high-speed interconnects for data centre networking and gave Invited and Tutorial talks at major conference venues. He has authored/co-authored more than 100 peer-reviewed papers including several post deadlines. He is currently a Member of Technical Staff and Research Engineer in Transmission and DSP in the Smart Network Fabric Lab, Nokia Bell Labs in Stuttgart, Germany.

Nicolás Abadía received the telecommunications engineering degree from the Technical University of Madrid, Spain; and the Royal Institute of Technology, Stockholm, Sweden. He received a joint M.Sc. degree from Ghent University, Belgium; Royal Institute of Technology, Sweden; and Free University of Brussels, Belgium, and the Ph.D. degree from the University of Paris-Sud, France. His doctoral thesis was done in collaboration with the research institute CEA-Leti, France. He was a joint Postdoctoral Fellow with Trinity College Dublin, Ireland; and McGill University, Canada. He is currently a Lecturer with the Cardiff University, Cardiff, U.K.; and the Institute for Compound Semiconductors, Cardiff, U.K. His research interests include optoelectronic devices and systems in III-V, silicon, and silicon nitride platforms for telecommunication and aerospace applications. He received several international recognitions such as the 2016 OSA Outstanding Reviewer Recognition, the SPIE Optics and Photonics Education Scholarship, and the Erasmus Mundus Scholarship; and national recognitions such as the Dr. César Milstein Grant and the best master thesis award by the Official College of Telecommunication Engineers and the Spanish Association of Telecommunication Engineers.

David V. Plant (F'07) received the Ph.D. degree from Brown University, Providence, RI, USA, in 1989. He was a Research Engineer with the University of California, Los Angeles, CA, USA, in 1989–1993, and has been a Professor with McGill University, Montreal, QC, Canada, since 1993, where he holds a James McGill Professorship. He has authored or coauthored more than 400 journal and conference papers and has one licensed patent. He has received five teaching awards and numerous other awards including the IEEE Photonics Society Engineering Achievement Award and the IEEE Microwave Theory and Techniques Society Microwave Prize. He is a Fellow of the Optical Society of America, the Royal Society of Canada, the Engineering Institute of Canada, and the Canadian Academy of Engineering. He currently holds a Killam Research Fellowship.